Bioactive Materials 36 (2024) 272–286

Contents lists available at ScienceDirect

Bioactive Materials

journal homepage: www.keaipublishing.com/en/journals/bioactive-materials

Self-adaptive pyroptosis-responsive nanoliposomes block pyroptosis in autoimmune inflammatory diseases

Kaiwang Xu [a,b,c,d,1], Huang Yang [e,1], Jinghua Fang [a,b,c,d,1], Kaijie Qiu [a,b,c,d], Haotian Shen [g], Guanrui Huang [g], Qiangqiang Zheng [h], Canlong Wang [a,b,c,d], Tengjing Xu [a,b,c,d], Xinning Yu [a,b,c,d], Jiajie Wang [a,b,c,d], Yunting Lin [a,b,c,d], Jiacheng Dai [a,b,c,d], Yuting Zhong [a,b,c,d], Hongyun Song [a,b,c,d], Sunan Zhu [a,b,c,d], Siheng Wang [a,b,c,d], Zhuxing Zhou [a,b,c,d], Guang Yang [a,b,c,d], Zhengwei Mao [e,f,*], Zongyou Pan [a,b,c,d,**], Xuesong Dai [a,b,c,d,***]

[a] Department of Orthopedic Surgery, Second Affiliated Hospital, School of Medicine, Zhejiang University, Hangzhou, 310009, China
[b] Orthopedics Research Institute, Zhejiang University, Hangzhou, 310009, China
[c] Key Laboratory of Motor System Disease Research and Precision Therapy of Zhejiang Province, Hangzhou, 310009, China
[d] Clinical Research Center of Motor System Disease of Zhejiang Province, Hangzhou, 310009, China
[e] MOE Key Laboratory of Macromolecular Synthesis and Functionalization, Department of Polymer Science and Engineering, Zhejiang University, Hangzhou, 310027, China
[f] Department of Hepatobiliary and Pancreatic Surgery, Second Affiliated Hospital, School of Medicine, Zhejiang University, Hangzhou, 310009, China
[g] Zhejiang University, Hangzhou, 310058, China
[h] Dr. Li Dak Sum & Yip Yio Chin Center for Stem Cells and Regenerative Medicine, Zhejiang University School of Medicine, Hangzhou, 310000, China

ARTICLE INFO

Keywords:
Nanoliposome
Pyroptosis
Autoimmune inflammatory diseases
Responsive drug delivery
Anti-inflammation

ABSTRACT

Nanoliposomes have a broad range of applications in the treatment of autoimmune inflammatory diseases because of their ability to considerably enhance drug transport. For their clinical application, nanoliposomes must be able to realize on-demand release of drugs at disease sites to maximize drug-delivery efficacy and minimize side effects. Therefore, responsive drug-release strategies for inflammation treatment have been explored; however, no specific design has been realized for a responsive drug-delivery system based on pyroptosis-related inflammation. Herein, we report a pioneering strategy for self-adaptive pyroptosis-responsive liposomes (R8-cardiolipin-containing nanoliposomes encapsulating dimethyl fumarate, RC-NL@DMF) that precisely release encapsulated anti-pyroptotic drugs into pyroptotic cells. The activated key pyroptotic protein, the *N*-terminal domain of gasdermin E, selectively integrates with the cardiolipin of liposomes, thus forming pores for controlled drug release, pyroptosis, and inflammation inhibition. Therefore, RC-NL@DMF exhibited effective therapeutic efficacies to alleviate autoimmune inflammatory damages in zymosan-induced arthritis mice and dextran sulfate sodium-induced inflammatory bowel disease mice. Our novel approach holds great promise for self-adaptive pyroptosis-responsive on-demand drug delivery, suppressing pyroptosis and treating autoimmune inflammatory diseases.

1. Introduction

Autoimmune inflammatory diseases result from the body's immune response to self-antigens, leading to tissue damage, and affect over 4% of the world's population [1,2]. Rheumatoid arthritis (RA) and inflammatory bowel disease (IBD) are the most representative autoimmune

Peer review under responsibility of KeAi Communications Co., Ltd.
* Corresponding author. MOE Key Laboratory of Macromolecular Synthesis and Functionalization, Department of Polymer Science and Engineering, Zhejiang University, Hangzhou, 310027, China.
** Corresponding author. Department of Orthopedic Surgery, Second Affiliated Hospital, School of Medicine, Zhejiang University, Hangzhou, 310009, China.
*** Corresponding author. Department of Orthopedic Surgery, Second Affiliated Hospital, School of Medicine, Zhejiang University, Hangzhou, 310009, China.
E-mail addresses: zwmao@zju.edu.cn (Z. Mao), panzongyou@zju.edu.cn (Z. Pan), daixshz@zju.edu.cn (X. Dai).
[1] These authors contributed equally to this work.

https://doi.org/10.1016/j.bioactmat.2024.02.022
Received 21 November 2023; Received in revised form 3 February 2024; Accepted 19 February 2024

inflammatory diseases [3,4]. Various small-molecule drugs, such as glucocorticoids and biological agents, have been developed for RA and IBD treatment [5,6]. However, these drugs are difficult to satisfy clinical demand because of low bioavailability and severe side effects, including gastrointestinal problems, medication resistance, and the possibility of malignant tumors [7,8]. Thus, it is imperative to develop drug-delivery systems with specific release abilities for enhancing bioavailability and minimizing side effects [9].

According to pathogenic alterations in inflammatory disorders, several bioresponsive drug-delivery systems have been meticulously designed over the past few decades, like pH-, redox-, and enzyme-responsive materials [10]. However, these bioresponsive drug-release systems are hindered by several obstacles, like low drug-release sensitivity and specificity, which restrict their clinical application [11]. For instance, pH-responsive materials have been heavily investigated owing to the acidic extracellular environment in inflammation [12]. However, most responsiveness of the pH-responsive materials was investigated at pH < 6 *in vitro*, which may not always correspond to the pH values in the *in vivo* inflammatory microenvironment (pH 6.5–6.7), leading to a diminished sensitivity in drug release [13,14]. In addition, the nonspecific off-target release could be caused by the distribution of acidic endosomes in normal cells [15]. Thus, it is time to develop a novel bioresponsive drug-delivery system for sensitive and specific drug release by exploiting a responsive signal that closely aligns with the pathological mechanisms of the disease.

Pyroptosis is a recently discovered form of programmed cell death that is closely associated with inflammation [16,17]. It is characterized by gasdermin-mediated membrane pore formation, subsequent cellular lysis, and inflammatory cytokine release [18,19]. Gasdermin D (GSDMD) is the most comprehensively studied member of the gasdermin family, being cleaved by caspases 1, 4/5, 8, and 11, thereby inducing pyroptosis [20,21]. Similar to GSDMD, recent advancements in pyroptosis research have revealed a new mechanism of gasdermin E (GSDME)-mediated pyroptosis, primarily activated by caspase-3, resulting in the transition from noninflammatory apoptosis to inflammatory pyroptosis [22]. Due to the highly proinflammatory characteristic of GSDME, GSDME-mediated cell pyroptosis plays a more pivotal role in triggering immune inflammatory responses and driving the pathogenesis of autoimmune inflammatory diseases, such as RA and IBD [23–25]. Studies have also reported that when cells initiate pyroptosis, a substantial amount of the *N*-terminal domain of GSDME (GSDME-N) is activated intracellularly, which binds to cardiolipin (CL) in the inner leaflet of cell membranes and forms pores [17]. Inspired by this, GSDME-N has been shown to efficiently bind to CL-containing liposomes and form pores on their membranes, releasing their contents [22,26]. Therefore, utilizing the novel inflammatory pathogenic target GSDME as a responsive signal offers a promising strategy for bioresponsive drug delivery.

To our knowledge, we designed for the first time a GSDME-N-responsive nanoliposome drug-delivery system (RC-NL@DMF) that targets cell pyroptosis. The system contains CL and R8 to achieve the pyroptosis-responsive release of dimethyl fumarate (DMF), a clinically approved anti-pyroptosis agent (Fig. 1A) [27,28]. During the pyroptosis, the GSDME-N activated by caspase-3 integrates with the CL on the liposome surface, inducing pore formation and thereby initiating the pyroptosis-responsive release of DMF. Moreover, incorporating the R8 cell-penetrating peptide facilitates the cellular uptake of liposomes, enabling them to respond more effectively to intracellular pyroptotic signals and maximize their responsive drug-release capability (Fig. 1C) [29,30]. We attempted to validate the pyroptosis-responsive drug-release capability of RC-NL@DMF and clarify its specific drug-release characteristics. Furthermore, our study confirmed that RC-NL@DMF can significantly inhibit pyroptosis and inflammation by suppressing the caspase-3/GSDME pathway activation in macrophages. Finally, the

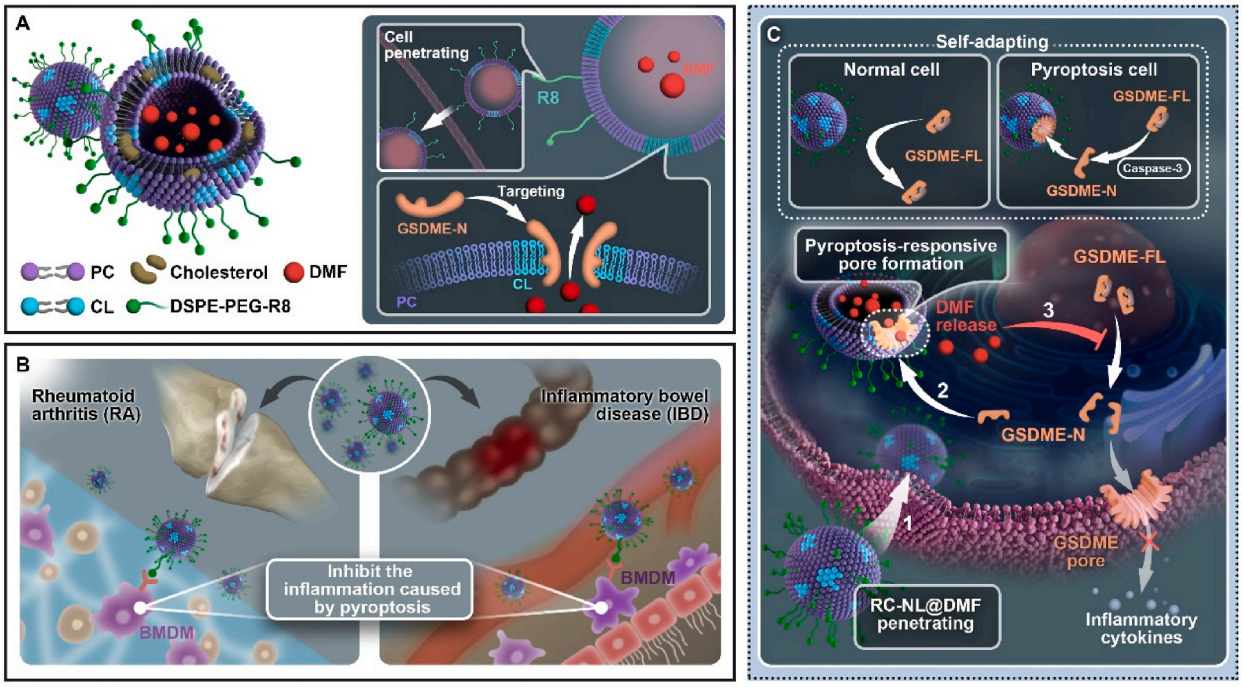

Fig. 1. Schematic illustration of self-adaptive pyroptosis-responsive nanoliposomes (RC-NL@DMF) blocking pyroptosis in autoimmune inflammatory diseases. A) Structure of RC-NL@DMF and characterization of its pyroptosis-responsive drug-release functionality; B) RC-NL@DMF treats pyroptosis-related autoimmune inflammatory diseases by suppressing pyroptosis in macrophages and attenuating inflammation resulting from pyroptosis; and C) Schematic illustration of pyroptosis-responsive pore formation for drug release in the pyroptotic cells. This objective is spirited into three folds: 1) Pyroptosis-responsive liposomes efficiently penetrate the cells, facilitated by the action of the R8 cell-penetrating peptide; 2) Once pyroptosis occurs, the activated GSDME-N selectively binds to the CL on the liposome's surface, creating pores for the encapsulated drug release; and 3) DMF, a classical pyroptosis inhibitor, exerts its pyroptosis-inhibiting effects and subsequent inflammatory response attenuation by inhibiting the caspase 3/GSDME pathway.

anti-inflammatory and therapeutic efficacies of RC-NL@DMF were demonstrated in mouse models of zymosan-induced arthritis (ZIA) and dextran sulfate sodium (DSS)–induced IBD, which are commonly used models of autoimmune inflammatory diseases (Fig. 1B). The self-adaptive pyroptosis-responsive nanoliposome drug-delivery system may be applicable for various inflammatory diseases and provides a novel approach for drug delivery in clinical applications.

2. Results and discussion

2.1. Preparation and characterization of RC-NL@DMF

Recent studies have identified that the GSDME-N can bind cell membrane lipids and pores on the membrane surface, and CL is the main target of GSDME-N [17]. Therefore, if CL is added to basic phosphatidylcholine liposomes, GSDME-N can efficiently bind CL-containing liposomes, poring the surface and releasing the contents. Moreover, considering that the GSDME-N is mainly distributed inside the cell, we added a common cell-penetrating peptide, R8, on the liposome surface to enable a more efficient liposome entry into cells. We initially designed a self-adaptive liposome responsive to the intracellular pyroptotic microenvironment, culminating in discovering pyroptosis-responsive drug-release properties.

The pyroptosis-responsive liposomes (RC-NL@DMF) were prepared using the conventional filming-rehydration method. The individual component ratio in the liposomes was also optimized. First, we discussed the proportion of R8 cell-penetrating peptides. Liposomes modified with a high R8 density (5 mol %) were primarily internalized via macropinocytosis and were less subject to lysosomal degradation [30]. Therefore, we further investigated the impact of R8 on the cellular uptake of hydrophilic drugs. To this end, fluorescein sodium salt (FSS, a hydrophilic dye) was encapsulated into liposomes with and without R8 (RC-NL@FSS and C-NL@FSS) using the film dispersion method. As revealed by confocal microscopy images (Figs. S1A and B), free FSS was poorly taken up by cells within a short period. In contrast, R8 significantly improved the cellular uptake efficiency of hydrophilic drugs.

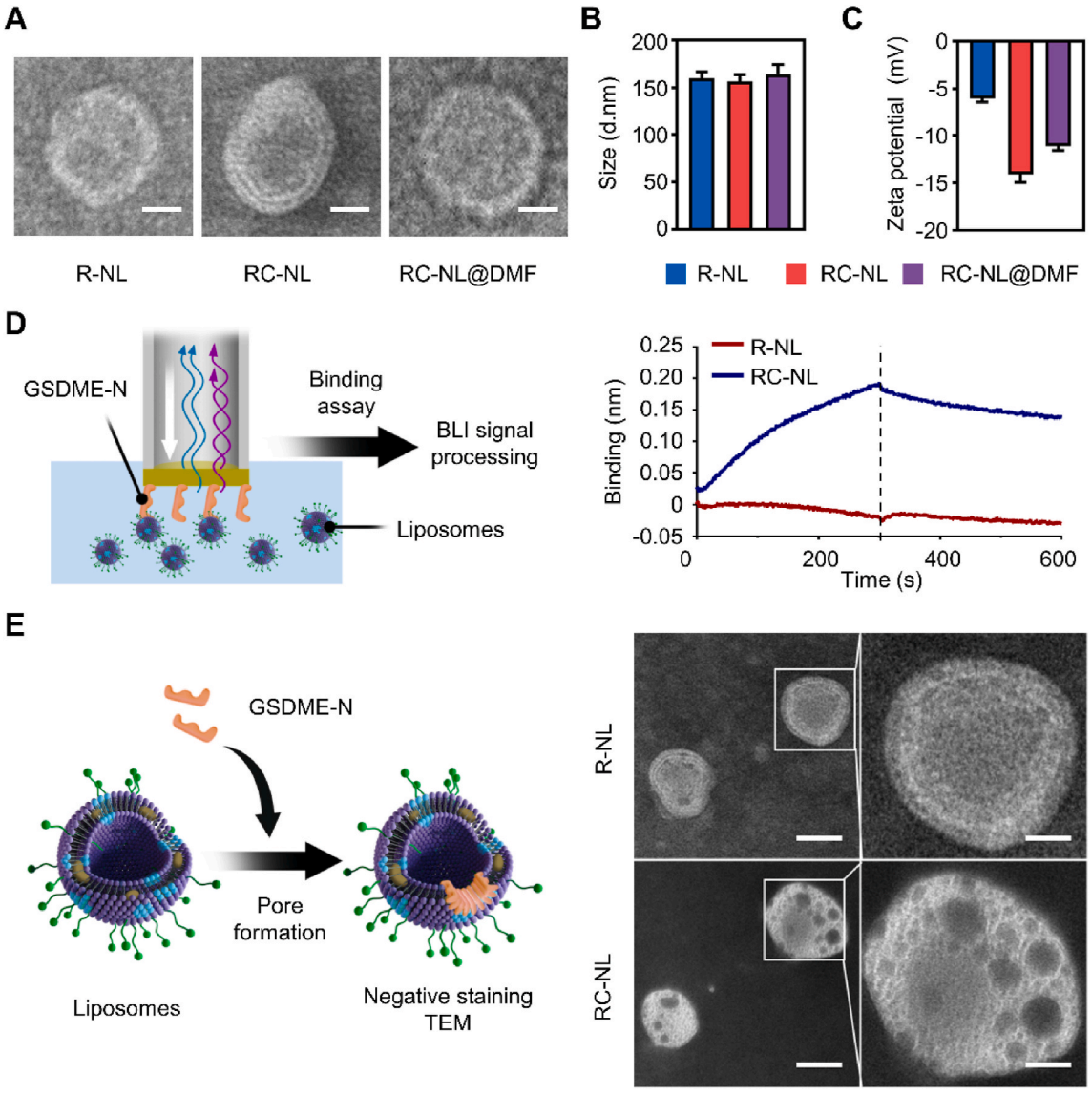

Fig. 2. Characterization of RC-NL@DMF and its pyroptosis-responsive pore formation function triggered by the GSDME-N protein. (A) Transmission electron microscopy images of R-NL, RC-NL, and RC-NL@DMF after negative staining. Scale bars, 50 nm; (B, C) Size and zeta potential of R-NL, RC-NL, and RC-NL@DMF (n = 3); (D) Association curves of liposomes and the GSDME-N protein. SA biosensor was loaded with the GSDME-N protein. (E) Liposomes were treated with the GSDME-N protein. The liposomes are depicted in representative negative-stain electron micrographs. Scale bars, 150 nm. Enlarged scale bars, 50 nm. All data are representative of three independent experiments.

Consequently, macrophages internalized drugs to a greater extent and exhibited more efficient responsive drug-release capability within the cells. To attain optimal pyroptosis-responsive drug-release capability, we investigated the CL optimal ratio in liposome systems. Calcein-encapsulated liposomes with varying CL ratios were prepared, and through the calcein release assays, we discovered that the content leakage from different liposomes increased with increasing CL content. However, when the CL ratio exceeded 20%, there was no significant alteration in the leakage rate (Fig. S2). Thus, we determined that the optimal CL content was 20%.

After optimizing the proportion of each component in RC-NL, we optimized the DMF loading efficiency. The DMF loading efficiency in liposomes was assessed using the dialysis method by varying the DMF amount while keeping the liposome amount constant (Fig. S3). When the DMF input amount was 0.5 mg, the DMF loading efficiency in liposomes was 5.93% ± 0.75%. With an increase in the DMF input amount to 1 mg, the loading efficiency increased to 15.07% ± 1.33%. However, further increasing the input amount to 1.5 mg did not significantly increase loading efficiency (15.40% ± 2.10%). Therefore, we used 1 mg of DMF input for further investigations.

As shown in Fig. 2A and B, after extrusion using a 200-nm filter, the three prepared liposomes exhibited similar bubble structures under transmission electron microscopy and comparable sizes measured using dynamic laser light scattering (DLS). The zeta potential of the RC-NL changed from −5.87 ± 3.94 mV to −13.1 ± 6.12 mV with the addition of negatively charged CL (Fig. 2C). The polydispersity index (PDI) of the R8-containing nanoliposomes (R-NL) was 0.132 ± 0.036, that of the R8-cardiolipin-containing nanoliposomes (RC-NL) was 0.133 ± 0.047, the RC-NL@DMF was 0.146 ± 0.048, indicating that liposomes were homogeneous and stable (Fig. S4). The long-term stability of R-NLs, RC-NLs, and RC-NL@DMFs was evaluated, and all nanoliposomes showed negligible changes in size over one week (Fig. S5). Finally, stable liposome systems were obtained for future studies.

2.2. *Pyroptosis-responsive pore-forming drug-release capability of RC-NL@DMF*

To demonstrate the broad applicability of the pyroptosis-responsive pore formation function of RC-NL@DMF, we first assayed the binding of recombinant GSDME-N to liposomes. Bio-layer interferometry (BLI) represented a label-free analytical methodology for conducting real-time protein interaction analysis. Furthermore, the use of BLI could be extended to investigate protein–liposome interactions. In this study, we immobilized the recombinant GSDME-N onto the biosensor surface and subsequently exposed the sensor to the liposomes of interest. Subsequently, the binding of these liposomes to the protein led to a distinct alteration in the optical signal, which was then detected by the biosensor. The individual association curves are shown in Fig. 2D. It was observed that RC-NLs were significantly bound to GSDME-N, while R-NLs showed no such binding.

Moreover, to better visualize how GSDME-N works on RC-NL, negative-stain electron microscopy revealed multiple pores on nearly all RC-NLs incubated with the GSDME-N (Fig. 2E). However, the R-NLs did not show any pores. Our results indicated that RC-NLs were effective for pore formation triggered by the pyroptotic protein GSDME-N.

Subsequently, we investigated the GSDME-*N*-driven triggering of content release from RC-NL. For these studies, we used the calcein release assay and created calcein-encapsulated liposomes (Fig. 3A). According to the kinetic curves in Fig. 3B, when treated with 5-μM GSDME-N, RC-NL promoted approximately 60% calcein dye release within 5 min, whereas R-NL lacking CL showed only minimal background release. The drug release behavior of DMF from different liposomes, with or without GSDME-N treatment, also exhibited similar drug release curves (Fig. S6). Then, we investigated calcein release from liposomes under conditions that more closely resemble the intracellular microenvironment during pyroptosis. Calcein-loaded liposomes were incubated with the addition of concentrated pyroptotic cell lysate.

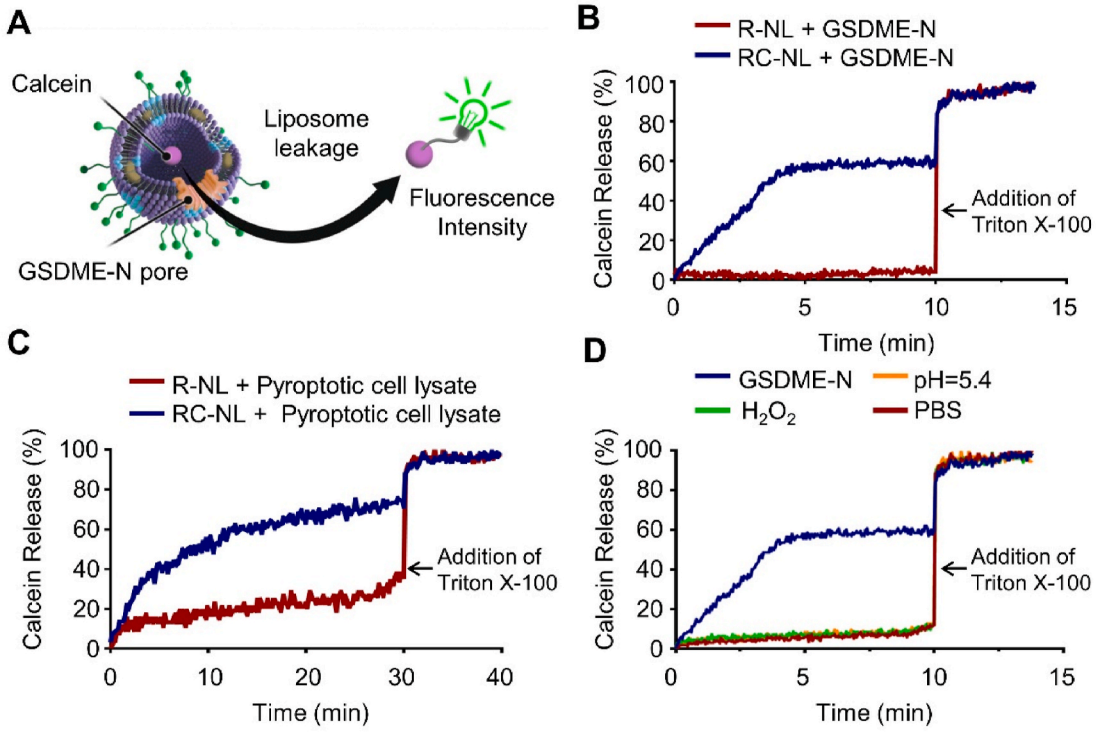

Fig. 3. Assessment of triggered cargo release from pyroptosis-responsive liposomes. (A) Schematic illustration of the pyroptosis-related calcein dye release assay; (B) Kinetic calcein release curves for R-NL and RC-NL after adding GSDME-N; (C) Kinetic calcein release curves for R-NL and RC-NL after adding concentrated pyroptotic cell lysate; (D) Kinetic calcein release curves for RC-NL after adding GSDME-N, phosphate-buffered saline (PBS), acidic stimulation, and ROS stimulation. After the fluorescence achieved a plateau, Triton X-100 detergent was applied to induce 100% release. All data are representative of three independent experiments.

Pyroptotic cell lysate significantly increased the calcein cumulative release from RC-NL compared with R-NL (Fig. 3C), confirming that RC-NL possessed efficient and sensitive pyroptosis-responsive drug-release capabilities.

To further investigate the RC-NL specificity for GSDME-N, we separately introduced other common inflammatory microenvironmental signals into calcein-encapsulated RC-NL, such as acidity (pH = 5.4) and reactive oxygen species (H_2O_2). As shown in Fig. 3D, calcein within RC-NL responded to release only under the stimulation of GSDME-N, while it remained entrapped in RC-NL in the presence of PBS, acidic stimulation, and reactive oxygen species stimulation. This indicates that RC-NL exhibits excellent pyroptosis-responsive specificity. Finally, we explored

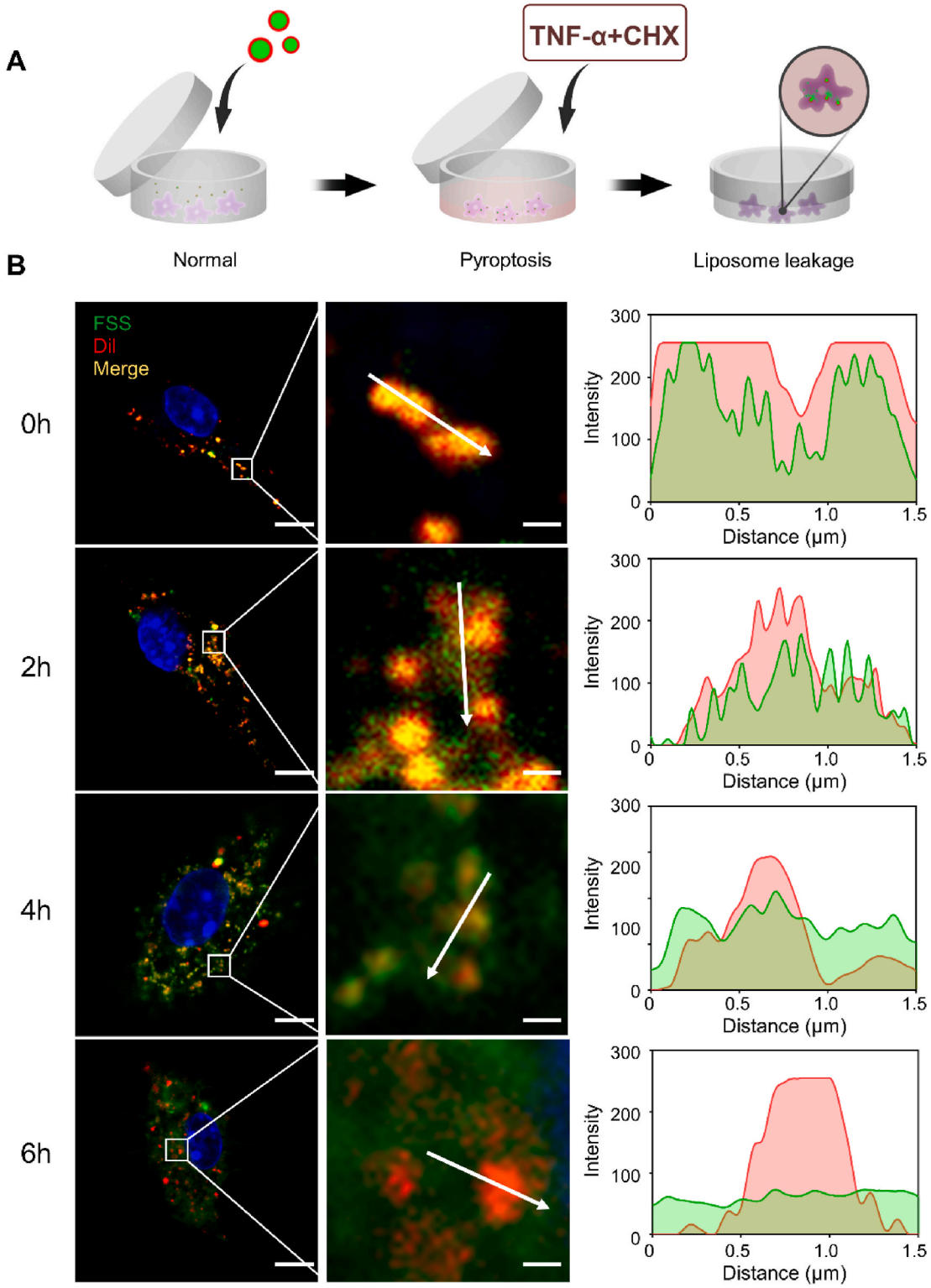

Fig. 4. Pyroptosis-responsiveness of RC-NL in the pyroptotic cells. (A) Schematic illustration of the intracellular pyroptosis-responsive release monitoring experiment; (B) Fluorescence leakage images of RC-NL in pyroptotic cells at different times (0–6 h). Intensity profiles across the cell along the white arrow. Scale bars, 5 μm. Enlarged scale bars, 0.5 μm. Dil, red; nuclei, blue; fluorescein sodium salt (FSS), green. All data presented are representative of three independent experiments.

the release characteristics of pyroptosis-responsive liposomes under different levels of pyroptosis stimulation, using 5- and 10-μM GSDME-N as stimuli. As shown in Fig. S7, different rates of calcein release were observed under varying degrees of GSDME-N stimulation, with higher concentrations of pyroptotic stimulation resulting in faster calcein release.

The above experiments were performed *in vitro* by adding recombinant GSDME-N protein to explore the ability of pyroptosis-responsive drug release; however, they were not demonstrated in living cells. To investigate the drug-release capability of the loaded liposomes in the cellular pyroptotic response, liposomes labeled with 1,1′-dioctadecyl-3,3,3′,3′-tetramethylindocarbocyanine perchlorate (Dil, a membrane red fluorescent dye) encapsulating FSS were co-cultured with bone-marrow-derived macrophage (BMDM) for 2 h, followed by the addition of 20-ng/mL tumor necrosis factor-alpha (TNF-α) and 10-μg/mL cycloheximide (CHX) to simulate cellular pyroptosis. After 6 h, the release behavior of the drug in cells was simulated by monitoring the fluorescence signals of Dil and FSS using confocal microscopy (Fig. 4A). According to fluorescence merged images and distribution along white arrows (Figs. S8A and B), the fluorescence signals of Dil and FSS in R-NL showed distinct co-localization, with only a small amount of FSS fluorescence signal leaking out. In contrast, the FSS fluorescence signal in RC-NL leaked extensively from the Dil signal, resulting in a dispersed distribution within the cells. Intrigued by this phenomenon, we further examined the complete drug-release characteristics of RC-NL during whole-cell pyroptosis. As anticipated, with the progression of time, the FSS signal gradually leaked from the Dil signal, expanding in area and eventually dispersing throughout the entire cell (Fig. 4B). However, the fluorescence signals of Dil and FSS in R-NL exhibited distinct co-localization during cell pyroptosis (Fig. S9). These results indicated that RC-NL was responsive to GSDME-N and capable of responding to pyroptotic cells by releasing drugs through pore formation.

2.3. RC-NL@DMF decreased pyroptosis by inhibiting the caspase-3/GSDME signaling pathway

Ahead of *in vitro* BMDMs protection studies, live/dead cell staining assays were used to evaluate the viability of BMDMs incubated with RC-NL, R8-containing nanoliposomes encapsulating DMF (R-NL@DMF), and RC-NL@DMF at concentrations of 0.01, 0.02, 0.05, 0.1, and 0.2 mg/mL for 24 h. The results revealed that the liposomes had no significant cytotoxicity at the indicated concentration (Fig. S10A). Next, to achieve optimal pyroptosis inhibition capability in therapeutic studies, we explored the optimum dosage within the liposome systems. During pyroptosis, GSDME-N is embedded in the cell membrane, creating pores that lead to cellular rupture and cytosolic content release, elevating the presence of stable cytosolic enzyme lactate dehydrogenase (LDH). Therefore, we utilized the extent of LDH release as an indicator to assess the degree of pyroptosis. BMDMs were pretreated with RC-NL@DMF at concentrations of 0.01, 0.02, 0.05, 0.1, and 0.2 mg/mL and subsequently stimulated with TNF-α and CHX to induce pyroptosis. We observed that the extent of LDH release inhibition increased with the increasing dose. However, when the concentration exceeded 0.1 mg/mL, there was no significant alteration in the degree of LDH release (Fig. S10B). Thus, we determined that the optimal dose was 0.1 mg/mL.

To assess the efficacy of pyroptosis inhibition *in vitro*, BMDMs were pretreated with free DMF or liposomes (RC-NL, R-NL@DMF, and RC-NL@DMF) at 0.1 mg/mL and subsequently stimulated with TNF-α and CHX to induce pyroptosis (Fig. 5A). RC-NL@DMF pretreatment reduced LDH release compared with the TNF-α-stimulated group, revealing that plasma membrane leakage was prevented (Fig. 5B). Additionally, interleukin (IL)-1β is essential for activating cell pyroptosis, associated with the severity of inflammatory conditions [24]. TNF-α-induced macrophages had higher levels of IL-1β expression than control macrophages. The RC-NL@DMF pretreatment significantly reduced IL-1β expression and exceeded the other groups, including DMF, RC-NL, and R-NL@DMF (Fig. 5C).

Subsequently, we measured the expression of pyroptosis-associated proteins using western blotting analysis. As illustrated in Fig. 5D–F, BMDMs treated with TNF-α and CHX exhibited increased expression of GSDME-N and cleaved caspase-3. Pretreatment with RC-NL@DMF significantly inhibited the expression of these pyroptosis-related proteins and exhibited superior efficacy compared with other groups, including DMF, RC-NL, and R-NL@DMF.

Furthermore, pyroptosis is typically characterized by the expansion of cells forming large ballooning bubbles before the cell membrane ruptures. TNF-α-stimulated BMDMs showed a significant presence of clear ballooning bubbles (black arrows), while the BMDMs treated with RC-NL@DMF exhibited only a limited number of pyroptotic morphological characteristics (Fig. S11). Moreover, the pyroptotic cell populations were demonstrated using annexin V and propidium iodide (PI) double staining because of the plasma membrane leakage, which causes PI permeability, and phosphatidylserine externalization, which causes them to stain with annexin V [31,32]. The confocal microscopy fluorescence images and the flow cytometry results validated that the pyroptotic cells that were annexin V and PI double positive were significantly decreased by the RC-NL@DMF treatment (Fig. 5G–I).

The results showed the superior pyroptosis-inhibiting potential of RC-NL@DMF *in vitro*, which can be attributed to its pyroptosis-responsive drug-release capability. We also observed that RC-NL without loaded drugs exhibited therapeutic effects compared with the control group, even though it did not suppress the expression of pyroptosis-associated proteins in Western blot analysis. This could be attributed to its function as a “nanobait” that competitively binds to the pyroptosis key molecule GSDME-N within cells, thereby reducing the incidence of pyroptosis.

2.4. Therapeutic efficacy of RC-NL@DMF in ZIA mice

Before conducting *in vivo* therapeutic experiments, we assessed the systematic toxicity of the liposomes after treatment through intravenous injection. Blood erythrocytes, leukocytes, and hemoglobin did not significantly vary between groups (Fig. S12). Moreover, the analysis of hematoxylin-eosin (HE) staining of the major organs, including the heart, liver, spleen, lung, and kidney, revealed no evident histopathological changes (Fig. S13). These results suggested that liposomes were highly biocompatible *in vivo* and suitable for therapeutic application.

Inspired by the effects of RC-NL@DMF on inhibiting pyroptosis and inflammation *in vitro*, we explored their therapeutic potential in a ZIA mouse model. ZIA mice are a model of RA that combines acute inflammation and pyroptosis activation, leading to significant joint destruction. We first determined the therapeutic efficacy of liposomes in ZIA mice by monitoring the joint swelling for six days (three intra-articular injections of the indicated liposomes with one-day spaced injections) (Fig. 6A). After the zymosan injection, the right knee joint exhibited notable swelling that peaked four days later, indicating serious joint inflammation. Although the mice treated with RC-NL and R-NL@DMF slowed a certain degree of joint swelling, those treated with RC-NL@DMF reduced the zymosan-induced joint swelling to almost total alleviation, indicating a stronger ability of RC-NL@DMF to reduce joint inflammation (Fig. 6B).

Micro-computed tomography (Micro-CT) analysis was performed to evaluate bone and joint integrity. As revealed by the images of the right hind knee joints, the surface bone erosion of ZIA mice was notably diminished after RC-NL@DMF treatment, and the bone volume density largely recovered to the normal level (Fig. 6C and I). These findings indicated that RC-NL@DMF could effectively prevent bone loss in ZIA mice.

During the progression of RA, continuous inflammation contributes to the thickening of the synovial lining cell layer, massive inflammatory cell infiltration, and cartilage destruction, resulting in irreversible damage to the joint. As revealed by HE staining (Fig. 6D), synovium

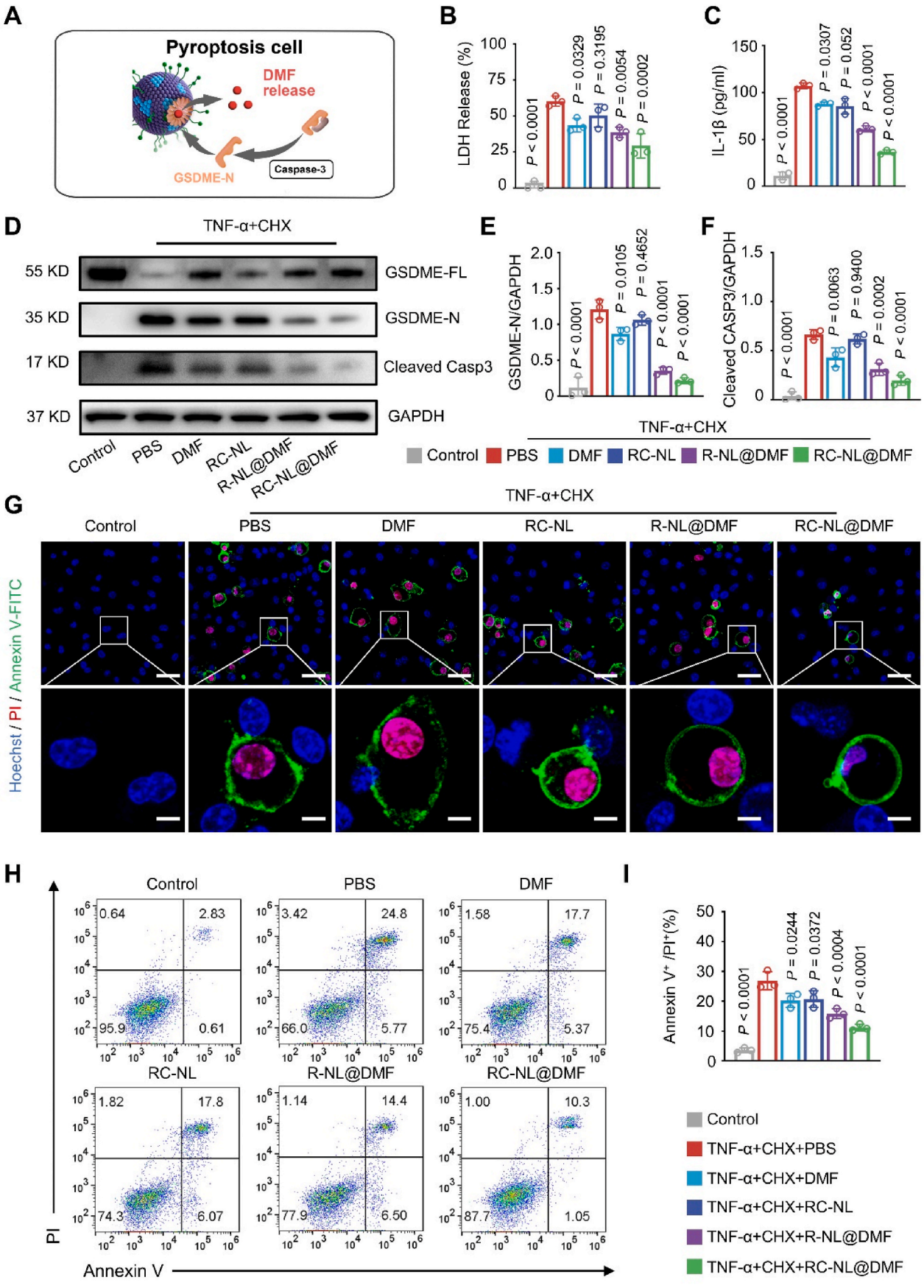

(caption on next page)

Fig. 5. RC-NL@DMF decreased pyroptosis by inhibiting the caspase-3/GSDME signaling pathway. (A) Schematic illustration of the pyroptosis-responsive drug release; (B) LDH and (C) IL-β release from BMDMs. BMDMs were pretreated with free DMF, RC-NL, R-NL@DMF, or RC-NL@DMF followed by TNF-α and CHX pyroptotic stimulation; (D) Western blot assays of the pyroptosis signaling pathway in BMDMs incubated with the indicated treatments and TNF-α and CHX pyroptotic stimulation. The experiments were repeated three times independently. (E) Quantification of GSDME-N; (F) Cleaved caspase-3 normalized to GAPDH levels ($n = 3$); (G) confocal images of the BMDMs incubated with the indicated treatments and pyroptotic stimulation. BMDMs were incubated with PI, annexin V-fluorescein isothiocyanate (FITC), and Hoechst 15 min before imaging. Scale bars, 20 μm; enlarged scale bars, 5 μm. (H, I) Flow cytometry of PI and annexin V-FITC-stained BMDMs. BMDMs were pretreated with the indicated treatments followed by pyroptotic stimulation. All presented data reflect three distinct experiments and are depicted as means ± standard deviation (SD). Statistical analysis was calculated using an unpaired student's two-sided *t*-test. All P denotes the statistical significance relative to the TNF-α + CHX + PBS group.

thickening and granulocyte infiltration were inhibited after RC-NL@DMFs treatment, conferring reduced histological scores (Fig. 6G). Furthermore, DMF and RC-NL-treated mice demonstrated a cartilage pattern similar to the model mice, with evident cartilage erosion and reduced cartilage thickness (Fig. 6E). However, after RC-NL@DMFs treatment, the knee joint displayed only minor signs of cartilage degradation, and the histological score was markedly lower than that in the other groups (Fig. 6H).

To validate the inhibitory effect of RC-NL@DMF on macrophages pyroptosis, we labeled the macrophage marker F4/80 (in red) and the key pyroptosis protein GSDME-N (in green). Immunofluorescence staining further confirmed the abundant expression of GSDME-N in the macrophages of the synovial tissue in ZIA mice. While RC-NL treatment did not impact GSDME activation, treatment with RC-NL@DMF significantly reduced the expression of GSDME-N in the macrophages (Fig. 6F and J). Our findings suggested that RC-NL@DMF could suppress GSDME-N signaling and alleviate articular inflammation in ZIA model mice. The pyroptosis-responsive drug-release feature of RC-NL@DMF enabled it to exhibit a potent inhibitory effect on the inflammation and pathogenesis of RA.

2.5. Therapeutic efficacy of RC-NL@DMF in DSS-induced IBD mice

To objectively evaluate the universal applicability of RC-NL@DMF, we tested its therapeutic effect in the mouse IBD model, which is another prevalent autoimmune inflammatory disorder model. Mice were fed 3% DSS in drinking water within days 0–7 and intravenously injected with PBS, DMF, RC-NL, R-NL@DMF, or RC-NL@DMF on days 3, 5, 7, and 9 (Fig. 7A).

First, to investigate the biodistribution of the liposomes, DiR-labeled RC-NL@DMF were intravenously injected in the IBD and sham mice. As shown in Fig. S14, IBD mice's inflamed colons revealed stronger fluorescence intensity than sham colons. These results demonstrated that liposomes possessed enhanced accumulation in the inflamed colons, possibly due to the passive targeting aggregation.

Furthermore, we observed a sustained weight loss in mice with DSS-induced IBD, which was significantly attenuated after treatment with RC-NL@DMF (Fig. 7B). Shortening of colon length is another characteristic symptom observed in DSS-induced IBD. As shown in Fig. 7C and F, DSS considerably reduced the colon length to 5.2 ± 0.20 cm, whereas RC-NL@DMF restored the colon length to 7.27 ± 0.21 cm, comparable to normal mice. The HE staining histological analysis further revealed that RC-NL@DMF treatment could safeguard the colonic epithelium against pathological damage and alleviate inflammatory cell infiltration (Fig. 7D, **G**). Finally, pyroptosis inhibition in the macrophages of colon was evaluated by immunofluorescence staining. Similarly, the level of GSDME-N expression in the macrophages of colon tissues treated with RC-NL@DMF was significantly lower than those treated with PBS (Fig. 7E, **H**). All these assessments once again highlighted the superior efficacy of RC-NL@DMF for the treatment of IBD, attributed to its highly efficient anti-pyroptosis drug-release capability in response to pyroptosis.

3. Conclusion

A self-adaptive pyroptosis-responsive nanoliposome system (RC-NL@DMF) has been developed for the on-demand release of anti-pyroptosis drugs to treat autoimmune inflammatory diseases. We systematically optimized the liposome composition to achieve the highest efficiency in pyroptosis-responsive drug release. Once pyroptosis occurred, the activated pivotal pyroptotic protein GSDME-N selectively bound to the surface CL of the liposomes, thereby creating pores for the controlled release of encapsulated DMF and restraining pyroptosis. The *in vivo* data showed that RC-NL@DMF exhibited effective therapeutic effects against the autoimmune inflammatory damage to the knee joints and colons in RA and IBD mice. Currently, studies on GSDME and autoimmune inflammatory diseases are predominantly focused on the mechanistic level, lacking direct application research. Our study aims to address this gap, highlighting the potential value of GSDME as a therapeutic target for autoimmune inflammatory diseases. This anti-pyroptosis drug-delivery approach provides a completely innovative paradigm for treating autoimmune inflammatory diseases. This approach achieves the specific release of drugs within pyroptotic cells while minimizing potential off-target effects and enhancing drug-delivery efficiency. Therefore, this strategy may be generalized to deliver various anti-pyroptosis drugs for intervening in pyroptosis to treat diverse autoimmune inflammatory diseases.

4. Materials and methods

4.1. Materials and reagents

Lecithin (B28313) and cholesterol (A10076) were purchased from Shanghai Yuanye Biotechnology (Shanghai, China). DSPE-PEG2K-R8 (R-D012) was purchased from Ruixi Biological Technology (Xian, China). TNF-α (410-MT) was purchased from R&D Systems (Minnesota, USA). CHX (HY-12320) and DiR (HY-D1048) were purchased from MCE (Shanghai, China). Enhanced BCA Protein Assay Kit (P0010S), lactate dehydrogenase (LDH), Cytotoxicity Assay Kit (C0016), 4′,6-diamidino-2-phenylindole (DAPI, C1006), Dil (C1991), calcein/PI cell viability/cytotoxicity assay kit (C2015), and cell counting kit-8 (C0037) were purchased from Beyotime (Shanghai, China). IL-1β Simple Step enzyme-linked immunosorbent assay kit (ab197742), anti-glyceraldehyde-3-phosphate dehydrogenase (GAPDH; ab8245), anti-GSDME (ab230482), anti-GSDME-N (ab215191), goat antirabbit IgG H&L (Alexa Fluor® 488) secondary antibodies (ab150081), and horseradish peroxidase-conjugated secondary antibodies (ab205718) were purchased from Abcam (Cambridge, UK). Anti-cleaved caspase-3 (Asp175) was purchased from Cell Signaling Technology (Boston, USA). Annexin V-FITC/PI apoptosis kit (AP101) was purchased from Liankebio (Hangzhou, China). Chemiluminescence ECL Western-blotting system and polyvinylidene fluoride membranes were purchased from Millipore (Bedford, MA, USA). CL (C0563), DMF (242926), calcein (C0875), FSS (F6377), zymosan A (Z4250), and dextran sodium sulfate DSS (42867) were purchased from Sigma-Aldrich (St Louis, USA). Anti-F4/80 (47-4801-82) and Goat anti-Rat IgG (H + L) Cross-Adsorbed Secondary Antibody (Alexa Fluor™ 555, A-21434) were purchased from Invitrogen (Calif, USA). Expression and purification of recombinant GSDME protein were conducted according to the recently described protocol [18], performed by Genscript (Nanjing, China). The recombinant active caspase 3 (ALX-201-059) was purchased from Enzo Life Sciences (New York, USA). PBS, H_2O_2, and bovine serum albumin were purchased from

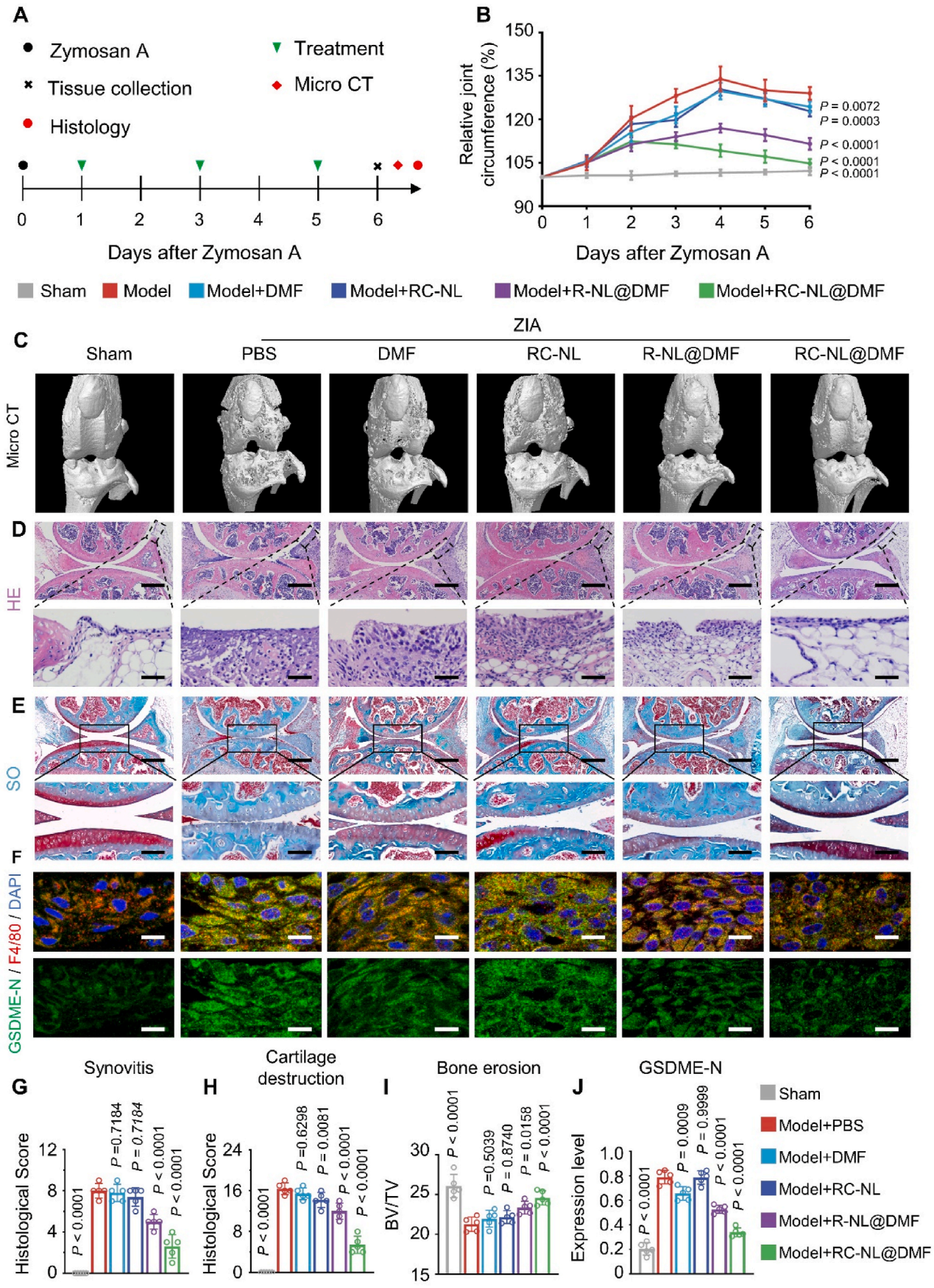

(caption on next page)

Fig. 6. The therapeutic effect of RC-NL@DMF in the ZIA mouse model. (A) Schematic illustration of the establishment and experimental schedule in mice; (B) Development of the relative right hind knee joint circumference. The knee joints' circumference on day 0 served as 100%; (C) Mice knee joints were scanned and 3D reconstructed using micro-CT to examine the joint shape and bone mass after the indicated treatments; (D, E) The morphology of articular cartilage (solid frame) and synovial (dotted frame) were observed by safranin O (SO) staining and HE staining of mice knee joints after the indicated treatments; (F) Representative fluorescent staining of knee joints labeled with anti-F4/80 (red), anti-GSDME-N (green), and DAPI (blue). Scale bars, 10 μm. Histological scores for (G) synovitis, (H) cartilage destruction, and (I) bone erosion. (J) Quantitation of GSDME-N expression level (pixels per unit area) in F4/80+ macrophages of the synovium. All presented data are reflective of five independent mice and are depicted as means ± standard deviation (SD). Statistical analysis was calculated by an unpaired Student's two-sided *t*-test. All P denotes the statistical significance relative to the ZIA Model + PBS group.

Sinopharm Chemical Reagent Co., Ltd (Beijing, China).

Male C57BL/6 mice (18–20 g, aged 6–8 weeks) were procured from the Animal Center at the Zhejiang Academy of Medical Sciences. The mice were housed and maintained under strict pathogen-free conditions at the Zhejiang Academy of Medical Sciences. All experimental procedures involving the mice were ethically reviewed and approved by the Committee of Zhejiang Center of Laboratory Animals (ZJCLA-IACUC-20020045).

4.2. Preparation and optimization of RC-NL@DMF

RC-NL@DMF was prepared according to previous studies [33]. Briefly, the liposomes were prepared using standard filming-rehydration techniques, including film formation, hydration, and extrusion through a 200-nm membrane. Then, 1-mg/mL soybean phospholipid, CL, cholesterol, and DSPE-PEG2K-R8 (R8) were separately prepared in chloroform. First, to fabricate R-NL, a mixture of soybean phospholipid: cholesterol: R8 in a molar ratio of 65:30:5 was prepared [29]. Then, 5 mL of the above mixture was added into a round flask and evaporated slowly to form a film using a rotary evaporator under low pressure. Subsequently, 5 mL of deionized (DI) water was added to the round flask and sonicated for 20 min in an ice water bath to obtain R-NL.

Then, to prepare and optimize pyroptosis-responsive liposomes (RC-NL), we introduced varying molar ratios of CL (0, 10, 20, and 30 mol %) using the previously mentioned method to generate a lipid film. Subsequently, 5 mL of calcein aqueous solution (1 mg/mL) was added to the round flask and sonicated to obtain calcein-encapsulated RC-NL. The optimal CL ratio was determined through calcein release assays (following the method described below).

After optimizing the composition proportions within RC-NL, we continued to refine the loading efficiency of DMF. Similarly, 5 mL of DI water containing varying amounts of DMF (0.5, 1.0, or 1.5 mg) was added to the flask and sonicated to obtain drug-encapsulated RC-NL@DMF. Variations in the input amounts of DMF were used to optimize the loading efficiency of DMF within the liposomes. To achieve even smaller liposome sizes, the solution was extruded 11 or 13 times through the 200-nm filter membranes via a liposome extruder. Then, the solution in the flask was dialyzed in DI water for 24 h to eliminate the unencapsulated DMF. Finally, the RC-NL@DMF were harvested and stored at 4 °C for subsequent applications.

4.3. Loading and release of DMF

The loading efficiency of DMF in RC-NL was determined using a UV–visible spectrophotometer [34]. Initially, a concentration gradient curve for DMF dissolved in DI water was established. The concentration of free DMF was determined using a dialysis method involving a dialysis membrane immersed in DI water, stirring at 50 rpm at 37 °C for 72 h. The DMF loading efficiency in RC-NL@DMF was calculated according to the following equation: loading efficiency (%) = (Mt − Mf)/Mn × 100%, where Mt is the total input amount of DMF, Mf is related to the free DMF amount detected in dialyzed DI water, and Mn is the total amount of nanoliposomes (RC-NL). The liposomes without DMF loading (RC-NL) and those without CL (R-NL@DMF) were prepared using the same method.

The release curves of DMF [35], R-NL@DMF and RC-NL@DMF with or without GSDME-N were analyzed by placing each substance in dialysis bags in 50 mL centrifuge tubes containing DI water. The samples were positioned on a shaker vibrating at 100 rpm, and subsequently, 0.5 mL of PBS was extracted at indicated time points for DMF concentration testing.

4.4. Nanoliposomes characterization

Nanoliposome size, PDI and shape were analyzed through DLS measurements (Nano ZS90, Malvern Instrument Ltd.) and TEM (JSM-6510 LV JEOL, Japan). The surface electrical properties of the different liposomes were characterized by determining the zeta potential (Nano ZS90, Malvern Instrument Ltd.). To assess the stability of the liposomes, they were stored in pH 7.4 PBS at 4 °C and measured using DLS for seven days.

4.5. Cellular uptake of hydrophilic drugs

BMDMs were cultured in confocal dishes for confocal microscopy analysis (DMI8, Leica). FSS was used as a drug mimic to simulate the behavior of hydrophilic drugs. Free FSS, *C*-NL@FSS, and RC-NL@FSS (each at an equivalent dose of 0.156-mg/mL DMF) were added to the culture medium. After co-incubation for 1 h, the cells were washed three times with PBS, stained with DAPI for 30 min, and then examined using confocal microscopy. The ImageJ software was used to quantify the mean fluorescence intensity per cell.

4.6. GSDME-N protein preparation

First, 10 μg of purified GSDME was incubated with two units of active caspase-3 for 60 min in a 25-μL reaction solution with 50-mM HEPES (pH 7.5), 3-mM EDTA, 150-mM NaCl, 0.005% (vol/vol) Tween-20, and 10-mM DTT to generate GSDME-N protein for subsequent *in vitro* functional studies [22].

4.7. Pyroptotic cell lysis solution preparation

BMDMs were cultured in a 10-cm cell culture dish 24 h before the stimulation. Cells were treated with 20-ng/mL TNFα and 10-μg/ml CHX for 6 h to induce pyroptosis activation. Approximately 1×10^7 cells were harvested and washed three times with 4 °C PBS. Then, cells were resuspended in 1 ml of PBS containing 1 × protease inhibitor cocktail. Ultrasonic disruption was performed using a sonicator with the following parameters: 20 kHz and 3 min (six cycles of 30s on, 30 s off) on ice. Following sonication, cell lysates were centrifuged at 14,000×*g* for 10 min at 4 °C. The resulting supernatants were collected for further concentration. Then, 200 μL of the cell lysate was loaded into the ultrafiltration centrifugal tube (Millipore, 10kd) and centrifuged at 4000×*g* for 15 min at 4 °C until the volume was reduced to approximately 20 μL.

4.8. Calcein release assay

Calcein release from the liposomes was assessed following the methodology described in a previous study [36]. Utilizing the previously described filming-rehydration techniques, we fabricated pyroptosis-responsive liposomes containing calcein (RC-NL) and non-pyroptosis-responsive liposomes containing calcein (R-NL). We

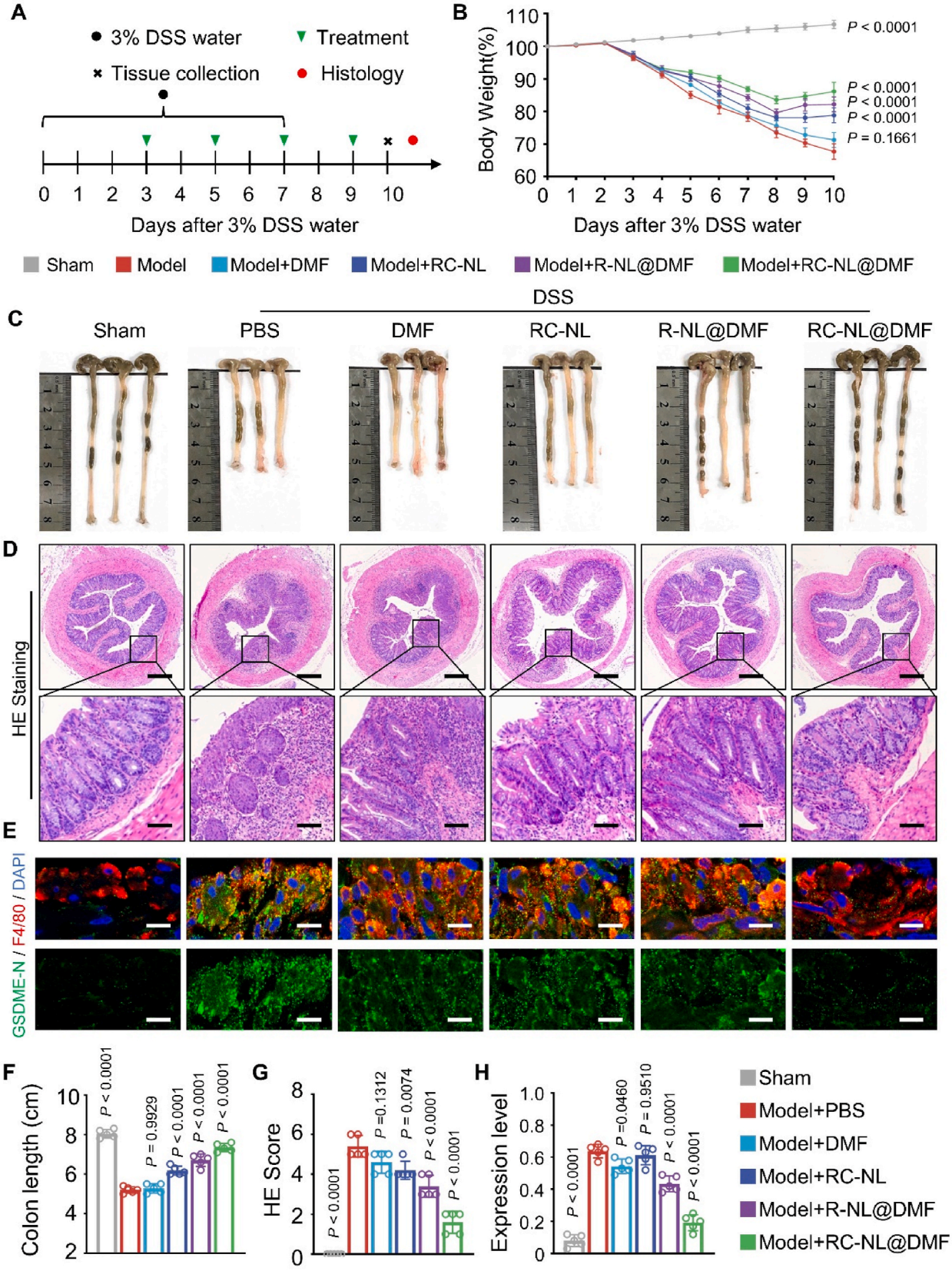

Fig. 7. The therapeutic effect of RC-NL@DMF in a DSS-induced IBD model. (A) Schematic illustration of the establishment and experimental schedule in the mice; (B) Changes in the relative body weight. Body weight on day 0 served as 100%. (C) Representative images of mouse colons in each group; (D) Representative HE staining images of colon sections; (E) Representative fluorescent staining of colons labeled with anti-F4/80 (red), anti-GSDME-N (green), and DAPI (blue). Scale bars, 10 μm; F) Colon length of mice; (G) Colonic damage scores according to HE staining were analyzed in each group; (H) Quantitation of GSDME-N expression level (pixels per unit area) in F4/80+ macrophages of the colons. All presented data are reflective of five independent mice and are depicted as means ± standard

deviation (SD). Statistical analysis was calculated using an unpaired student's two-sided *t*-test. All P denotes the statistical significance relative to the Model + PBS group.

determined the volumes of PBS, liposomal solution, and GSDME-N solution necessary to establish an assay with a total volume of 100 μL. Furthermore, we ensured that the ultimate concentrations of liposomes and GSDME-N are 500 μM and 5 μM, respectively, within a 100-μL solution. We added the assay components (without GSDME-N) to the wells of a 96-well solid black plate and set the excitation and emission wavelengths of the microplate reader to 490 nm and 520 nm (Spark, Tecan), respectively. Following an initial scan, GSDME-N solution was added to the well, and the fluorescence intensities were measured in kinetic mode over time. The assay was calibrated after completion by adding 1 μL of 20% Triton X-100 to break the liposomes and produce 100% release. The ratio of calcein released after time (t) was calculated according to Calcein Release (%) = $(I_t - I_0)/(I_{max} - I_0) \times 100\%$. I_0, It and I_{max} are the fluorescence intensities measured at the beginning of the assay, at time (t), and after the addition of Triton X-100. The same method was used to monitor the remaining stimuli assays.

4.9. BLI binding assay

BLI was performed on an Octet bio-layer interferometry instrument (ForteBio) [37,38]. Assays were performed in black 96-well plates at 37 °C. Before each test, biotinylated GSDME-N was attached to the streptavidin biosensor tips. Binding kinetics were monitored following immersion of the GSDME-*N*-bound biosensor tip in the indicated liposome formulations (R-NL or RC-NL) at a concentration of 500 μM. Association at each assay was conducted for 300 s. Finally, the dissociation was monitored with PBS for 300 s.

4.10. Electron microscopy assay

GSDME-N protein (5 μM) was incubated with the indicated liposomes (R-NL or RC-NL) (500 μM) at room temperature for 30 min. Subsequently, 5 μL of the mixture was transferred to carbon support films and negatively stained with 2% uranyl acetate. Samples were visualized with a transmission electron microscope.

4.11. Fluorescence leakage assay

Following the filming-rehydration method described above to prepare R-NL and RC-NL loaded with FSS, 10-μM Dil fluorescent solution was added. The mixture was incubated at room temperature for 20 min and dialyzed against DI water for 24 h. BMDMs were cultured in confocal dishes, and 50 μL of the dialyzed dual-fluorescent liposomes were co-incubated for 2 h. Then, 20-ng/mL TNF-α and 10-μg/mL CHX were added to simulate cellular pyroptosis. The experiment was terminated at the specified time. Cells were fixed with 4% paraformaldehyde and stained with DAPI. Finally, the release behavior of the drug in cells was simulated by monitoring the fluorescence signals of Dil (red) and FSS (green) using confocal microscopy.

4.12. Cellular cultivation

BMDMs were isolated from 6-week-old male C57/B6 mice. The mice were euthanized, and the femurs and tibias were collected. The bone marrow was flushed out with PBS. Cells were cultured in DMEM supplemented with 10% fetal bovine serum and macrophage colony-stimulating factor (25 ng/mL, Biolegend, USA). Nonadherent cells were removed after 24 h incubation to obtain a pure population of BMDMs. The medium was changed every two days, and the cells were passaged after reaching 80%–90% confluence.

4.13. Cellular treatment

BMDMs were cultured for seven days and treated with the indicated drugs overnight. Cells were washed three times with PBS to completely remove the free drugs. Then, BMDMs were treated with 20-ng/ml TNFα and 10-μg/ml CHX for 6 h to induce caspase-3/GSDME activation and pyroptosis.

4.14. LDH and IL-1β measurement

LDH release was analyzed using the LDH Cytotoxicity Assay Kit. IL-1β release was analyzed using IL-1β Simple Step enzyme-linked immunosorbent assay kit. BMDMs were seeded into 96-well plates and pretreated with the indicated drugs overnight. Then, the cells were transferred to a serum-free medium containing 20-ng/mL TNFα and 10-μg/mL CHX for 6 h. Cell culture supernatant was collected for further analysis. LDH or IL-1β release was analyzed according to the manufacturer's protocol and normalized to the release of untreated BMDMs.

4.15. Western blot assay

The levels of proteins, including cleaved caspase-3, GSDME-FL, GSDME-NT, and GAPDH, in BMDMs from different groups were detected using western blotting. Briefly, BMDMs were pretreated with the indicated drugs overnight and then incubated with 20-ng/mL TNFα and 10-μg/mL CHX for 6 h. Cells were then lysed in RIPA buffer with phenylmethylsulfonyl fluoride, and the protein concentration was determined using a BCA protein assay kit. Equal amounts of protein were separated using sodium dodecyl-sulfate polyacrylamide gel electrophoresis and transferred onto a polyvinylidene fluoride membrane. After blocking with protein-free rapid blocking buffer for 30 min at room temperature, primary antibodies against cleaved caspase-3, GSDME-FL, GSDME-NT, and GAPDH were incubated with the membrane overnight at 4 °C. The membrane was then incubated with secondary antibodies, and protein bands were detected using a chemiluminescence system. Finally, the blots were quantified with ImageJ software.

4.16. Annexin V-FITC/PI assay

The annexin V-FITC/PI assay was performed to evaluate pyroptosis, as previously described [31]. Briefly, cells were seeded into 6-well plates or confocal dishes and then pretreated with the indicated drugs overnight. After incubation with 20-ng/mL TNFα and 10-μg/mL CHX for 6 h, cells were stained with annexin V-FITC and PI according to the instruction manual. Fluorescence emission of annexin V-FITC and PI was quantified using flow cytometry (CytoFlex LX, Beckman) and confocal microscopy. Cells exhibiting positive signals for annexin V-FITC in green and PI in red were identified as pyroptotic cells.

4.17. Cell morphology assessment

BMDMs were pretreated with the indicated drugs overnight and then incubated with 20-ng/mL TNFα and 10-μg/mL CHX for 6 h to induce cell pyroptosis. Pyroptotic cells were visualized in bright field using optical microscopy (DM750, Leica). Large bubbles and cell swelling were considered to be typical features of pyroptosis [39].

4.18. Biosafety assay

To evaluate the cytotoxicity of the indicated liposomes, a live/dead cell viability assay was performed on BMDMs following a 24-h incubation with the indicated drugs. The proportion of live cells was

determined by analyzing fluorescence microscope images. Specifically, BMDMs were treated with the indicated concentrations of the indicated liposomes for 24 h. The relative viable cell numbers were then determined by measuring the optical density at 450 nm.

To assess the toxicity of liposomes *in vivo*, C57BL/6 mice were intravenously injected with the indicated drugs for a total of five injections, with a one-day interval between each injection. The control group received PBS. After five injections, blood samples and major organs, including the liver, kidney, lung, heart, and spleen, were collected. The major organs were fixed in a 4% paraformaldehyde solution, embedded in paraffin, and sectioned at a thickness of 4 μm. The tissue sections were stained with HE and examined under optical microscopy to assess any histological changes. Additionally, hematological analysis encompassed parameters such as red blood cell count, white blood cell count, and hemoglobin levels.

4.19. Treatment of ZIA mice

The ZIA model was established following previously reported methods [40,41]. First, 30 mg of zymosan A was resuspended in 2 mL of endotoxin-free saline, which was heated and homogenized using a sonic emulsifier. On day 0, a zymosan A solution (20 μL) was injected intra-articularly into the joint space of the right hind leg of C57BL/6 mice through the suprapatellar ligament. On days 1, 3, and 5 after the zymosan A injection, 10-μL PBS or 10-μL PBS containing various types of drugs (DMF, RC-NL, R-NL@DMF, or RC-NL@DMF, 1 mg/mL) was given via intra-articular injection into the right knee joint. Healthy mice without zymosan A injections or drug treatment served as the sham group.

4.20. Joint swelling

Every day (days 0–6), the right hind knee joint's circumference was measured to assess the swelling of the knee joints [42]. The electronic Vernier caliper measured the joint's two perpendicular diameters. $L = 2\pi b + 4(a - b)$, wherein a is the latero-lateral diameter and b is the antero-posterior diameter, was used to compute the circumference (L, cm). Results were expressed as the percentage of circumference immediately before injections. When measuring the joint swelling, the researcher was blinded to the group assignment.

4.21. Micro-CT

Micro-CT images were employed to assess the extent of knee joint damage and bone erosion in response to various therapeutic interventions, utilizing a micro-CT device (SKYSCAN 1278, Bruker). The collected data were processed to generate the three-dimensional structure of the joint (CTAN 3D image analysis). The bone volume density was analyzed using DATAVIEWER.

4.22. Histological analysis of knee joint

Upon sacrificing the mice, the right hind knees were carefully collected and fixed overnight in a 4% paraformaldehyde solution. The right hind knees were decalcified using a 10% EDTA solution for 50 days. Following decalcification, the knees were embedded in paraffin and sectioned into slices with a thickness of 4 μm. To visualize the tissue morphology, the sections were stained using HE and safranin O staining techniques. Histological images were acquired using a microscope (VS200, Olympus, Japan). The histological alterations related to synovial inflammation and cartilage destruction in the ankle joints were assessed using the Histopathological Scores of Synovia and Modified Osteoarthritis Research Society International scoring systems [43]. These scoring systems quantitatively evaluated the extent of synovial inflammation and cartilage damage observed in the histological sections. When performing the histological analysis, the researcher was blinded to the group assignment.

4.23. Immunofluorescence staining

Sections were washed with PBS, permeabilized with 0.2% Triton X-100 for 20 min, and blocked with 5% bovine serum albumin for 1 h at 37 °C. Sections were then incubated overnight at 4 °C with the primary antibody, followed by the cocktail containing fluorescent-labeled secondary antibodies for 1 h at room temperature. Nuclei were counterstained with DAPI for 15 min. Staining results were examined under a confocal microscope and quantified using ImageJ.

4.24. Treatment of IBD mice

To induce IBD, mice were administered 3% (w/v) DSS in their drinking water for one week [44]. On days 3, 5, 7, and 9, intravenous injections of PBS (100 μL), DMF, RC-NL, R-NL@DMF, or RC-NL@DMF (1 mg/mL, 100 μL) were administered to the mice ($n = 3$). Healthy mice without DSS challenges or treatments were in the sham group ($n = 3$). The mice body weight was monitored throughout the experimental period to assess disease changes.

4.25. Statistical analysis

Data are expressed as mean ± standard deviation (SD). Data were analyzed using SPSS (Ver 23.0, IBM Corp, USA) and graphed with GraphPad Prism (Ver 7.0, GraphPad Software Inc, USA). One-way analysis of variance (ANOVA), *t*-test, and Tukey's multiple comparisons test were utilized as appropriate. The significance level was presented as $^{*}P < 0.05$, $^{**}P < 0.01$, and $^{***}P < 0.001$.

Data availability

All data needed to evaluate the conclusions in the paper are present in the paper and/or the Supplementary Materials. Additional data related to this paper may be requested from the authors.

Ethics approval and consent to participate

All animal studies were performed with the approval of the ethical review board at the Committee of Zhejiang Center of Laboratory Animals (ZJCLA-IACUC-20020045). The animal experiment guidance from the ethical committee and the guide for care and use of laboratory animals were followed during the whole experiment course.

CRediT authorship contribution statement

Kaiwang Xu: Writing – original draft, Investigation, Conceptualization. **Huang Yang:** Writing – original draft, Investigation. **Jinghua Fang:** Methodology. **Kaijie Qiu:** Investigation. **Haotian Shen:** Methodology. **Guanrui Huang:** Formal analysis. **Qiangqiang Zheng:** Methodology. **Canlong Wang:** Methodology. **Tengjing Xu:** Formal analysis. **Xinning Yu:** Formal analysis. **Jiajie Wang:** Formal analysis. **Yunting Lin:** Investigation. **Jiacheng Dai:** Investigation. **Yuting Zhong:** Investigation. **Hongyun Song:** Investigation. **Sunan Zhu:** Formal analysis. **Siheng Wang:** Formal analysis. **Zhuxing Zhou:** Formal analysis. **Guang Yang:** Formal analysis. **Zhengwei Mao:** Writing – review & editing, Supervision, Conceptualization. **Zongyou Pan:** Writing – review & editing, Supervision, Conceptualization. **Xuesong Dai:** Writing – review & editing, Resources, Conceptualization.

Declaration of competing interest

The authors have no conflict of interests related to this publication.

Acknowledgments

The authors thank all the staff in the Key Laboratory of Motor System Disease Research and Precision Therapy of Zhejiang Province. This research was sustained by the National Natural Science Foundation of China (82072512, 52273152, 22161132027). Zhejiang Provincial Natural Science Foundation of China (LY23H060013, LY21H070001, LY20H160044, LBY21H060003). We thank Jingyao Chen from the core facility platform of Zhejiang University School of Medicine for the technical support.

Abbreviations

BLI	Bio-layer interferometry
BMDM	bone marrow-derived macrophages
C-NL	cardiolipin-containing nanoliposomes
CL	cardiolipin
CHX	cycloheximide
DI	deionized
DSS	dextran sodium sulfate
DMF	dimethyl fumarate
Dil	1,1′-dioctadecyl-3,3,3′,3′-tetramethylindocarbocyanine perchlorate
DLS	dynamic laser light scattering
HE	hematoxylin-eosin
FITC	fluorescein isothiocyanate
FSS	fluorescein sodium salt
GSDMD	gasdermin D
GSDME	gasdermin E
GSDME-N	the *N*-terminal domain of GSDME
IBD	inflammatory bowel disease
IL	interleukin
LDH	lactate dehydrogenase
n.s.	not significant
PBS	phosphate-buffered saline
PI	propidium iodide
RA	rheumatoid arthritis
R-NL	R8-containing nanoliposomes
R-NL@DMF	non-pyroptosis-responsive liposomes, R8-cardiolipin-containing nanoliposomes encapsulating dimethyl fumarate
RC-NL	R8-cardiolipin-containing nanoliposomes
RC-NL@DMF	pyroptosis-responsive liposomes, R8-cardiolipin-containing nanoliposomes encapsulating dimethyl fumarate
SO	safranin O
SD	standard deviation
TNF-α	tumor necrosis factor-alpha
ZIA	zymosan-induced arthritis

Appendix A. Supplementary data

Supplementary data to this article can be found online at https://doi.org/10.1016/j.bioactmat.2024.02.022.

References

[1] A. Zhernakova, S. Withoff, C. Wijmenga, Clinical implications of shared genetics and pathogenesis in autoimmune diseases, Nat. Rev. Endocrinol. 9 (11) (2013) 646–659.
[2] L. Wang, F.S. Wang, M.E. Gershwin, Human autoimmune diseases: a comprehensive update, J. Intern. Med. 278 (4) (2015) 369–395.
[3] R. Hodson, Inflammatory bowel disease, Nature 540 (7634) (2016) S97.
[4] M. Smith, J. Berman, What is rheumatoid arthritis? JAMA 327 (12) (2022) 1194.
[5] K. Kingsmore, A. Grammer, P. Lipsky, Drug repurposing to improve treatment of rheumatic autoimmune inflammatory diseases, Nat. Rev. Rheumatol. 16 (1) (2020) 32–52.
[6] D. Pisetsky, Pathogenesis of autoimmune disease, Nat. Rev. Nephrol. 19 (8) (2023) 509–524.
[7] L. van Ouwerkerk, A. Palmowski, I. Nevins, F. Buttgereit, P. Verschueren, J. Smolen, R. Landewé, J. Bijlsma, A. Kerschbaumer, R. Westhovens, T. Huizinga, C. Allaart, S. Bergstra, Systematic literature review of observational cohorts and clinical trials into the success rate of glucocorticoid discontinuation after their use as bridging therapy in patients with rheumatoid arthritis, Ann. Rheum. Dis. 81 (7) (2022) 937–943.
[8] S. Danese, L. Peyrin-Biroulet, IBD in 2013: enriching the therapeutic armamentarium for IBD, Nat. Rev. Gastroenterol. Hepatol. 11 (2) (2014) 84–86.
[9] J. Han, T. Sheng, Y. Zhang, H. Cheng, J. Gao, J. Yu, Z. Gu, Bioresponsive Immunotherapeutic Materials, Advanced Materials, Deerfield Beach, Fla., 2023 e2209778.
[10] R. Brusini, M. Varna, P. Couvreur, Advanced nanomedicines for the treatment of inflammatory diseases, Adv. Drug Deliv. Rev. 157 (2020) 161–178.
[11] Y. Dou, C. Li, L. Li, J. Guo, J. Zhang, Bioresponsive drug delivery systems for the treatment of inflammatory diseases, J. Contr. Release : official journal of the Controlled Release Society 327 (2020) 641–666.
[12] H. Ding, P. Tan, S. Fu, X. Tian, H. Zhang, X. Ma, Z. Gu, K. Luo, Preparation and application of pH-responsive drug delivery systems, J. Contr. Release : official journal of the Controlled Release Society 348 (2022) 206–238.
[13] J. Lou, J. Schuster, F. Barrera, M. Best, ATP-responsive liposomes via screening of lipid switches designed to undergo conformational changes upon binding phosphorylated metabolites, J. Am. Chem. Soc. 144 (8) (2022) 3746–3756.
[14] Z. Wang, S. Wang, K. Wang, X. Wu, C. Tu, C. Gao, Stimuli-sensitive nanotherapies for the treatment of osteoarthritis, Macromol. Biosci. 21 (11) (2021) e2100280.
[15] M. Hu, J. Chen, S. Liu, H. Xu, The acid gate in the lysosome, Autophagy 19 (4) (2023) 1368–1370.
[16] L. Tang, C. Lu, G. Zheng, B. Burgering, Emerging insights on the role of gasdermins in infection and inflammatory diseases, Clinical & translational immunology 9 (10) (2020) e1186.
[17] P. Broz, P. Pelegrín, F. Shao, The gasdermins, a protein family executing cell death and inflammation, Nat. Rev. Immunol. 20 (3) (2020) 143–157.
[18] J. Ding, K. Wang, W. Liu, Y. She, Q. Sun, J. Shi, H. Sun, D. Wang, F. Shao, Pore-forming activity and structural autoinhibition of the gasdermin family, Nature 535 (7610) (2016) 111–116.
[19] P. Vandenabeele, G. Bultynck, S. Savvides, Pore-forming proteins as drivers of membrane permeabilization in cell death pathways, Nat. Rev. Mol. Cell Biol. 24 (5) (2023) 312–333.
[20] N. Kayagaki, I. Stowe, B. Lee, K. O'Rourke, K. Anderson, S. Warming, T. Cuellar, B. Haley, M. Roose-Girma, Q. Phung, P. Liu, J. Lill, H. Li, J. Wu, S. Kummerfeld, J. Zhang, W. Lee, S. Snipas, G. Salvesen, L. Morris, L. Fitzgerald, Y. Zhang, E. Bertram, C. Goodnow, V. Dixit, Caspase-11 cleaves gasdermin D for non-canonical inflammasome signalling, Nature 526 (7575) (2015) 666–671.
[21] B. Burdette, A. Esparza, H. Zhu, S. Wang, Gasdermin D in pyroptosis, Acta Pharm. Sin. B 11 (9) (2021) 2768–2782.
[22] Y. Wang, W. Gao, X. Shi, J. Ding, W. Liu, H. He, K. Wang, F. Shao, Chemotherapy drugs induce pyroptosis through caspase-3 cleavage of a gasdermin, Nature 547 (7661) (2017) 99–103.
[23] X. Liu, S. Xia, Z. Zhang, H. Wu, J. Lieberman, Channelling inflammation: gasdermins in physiology and disease, Nat. Rev. Drug Discov. 20 (5) (2021) 384–405.
[24] Z. Zhai, F. Yang, W. Xu, J. Han, G. Luo, Y. Li, J. Zhuang, H. Jie, X. Li, X. Shi, X. Han, X. Luo, R. Song, Y. Chen, J. Liang, S. Wu, Y. He, E. Sun, Attenuation of rheumatoid arthritis through the inhibition of tumor necrosis factor-induced caspase 3/gasdermin E-mediated pyroptosis, Arthritis Rheumatol. 74 (3) (2022) 427–440.
[25] G. Tan, C. Huang, J. Chen, B. Chen, F. Zhi, Gasdermin-E-mediated pyroptosis participates in the pathogenesis of Crohn's disease by promoting intestinal inflammation, Cell Rep. 35 (11) (2021) 109265.
[26] S. Vasudevan, B. Behl, V. Rathinam, Pyroptosis-induced inflammation and tissue damage, Semin. Immunol. 69 (2023) 101781.
[27] F. Humphries, L. Shmuel-Galia, N. Ketelut-Carneiro, S. Li, B. Wang, V. Nemmara, R. Wilson, Z. Jiang, F. Khalighinejad, K. Muneeruddin, S. Shaffer, R. Dutta, C. Ionete, S. Pesiridis, S. Yang, P. Thompson, K. Fitzgerald, Succination inactivates gasdermin D and blocks pyroptosis, Science 369 (6511) (2020) 1633–1637.
[28] T. Ryan, A. Hooftman, A. Rehill, M. Johansen, E. Brien, J. Toller-Kawahisa, M. Wilk, E. Day, H. Weiss, P. Sarvari, E. Vozza, F. Schramm, C. Peace, A. Zotta, S. Miemczyk, C. Nalkurthi, N. Hansbro, G. McManus, L. O'Doherty, S. Gargan, A. Long, J. Dunne, C. Cheallaigh, N. Conlon, M. Carty, P. Fallon, K. Mills, E. Creagh, J. Donnell, P. Hertzog, P. Hansbro, R. McLoughlin, M. Wygrecka, R. Preston, Z. Zasłona, L. O'Neill, Dimethyl fumarate and 4-octyl itaconate are anticoagulants that suppress Tissue Factor in macrophages via inhibition of Type I Interferon, Nat. Commun. 14 (1) (2023) 3513.
[29] I. Khalil, K. Kogure, S. Futaki, H. Harashima, High density of octaarginine stimulates macropinocytosis leading to efficient intracellular trafficking for gene expression, J. Biol. Chem. 281 (6) (2006) 3544–3551.
[30] I. Nakase, H. Akita, K. Kogure, A. Gräslund, U. Langel, H. Harashima, S. Futaki, Efficient intracellular delivery of nucleic acid pharmaceuticals using cell-penetrating peptides, Acc. Chem. Res. 45 (7) (2012) 1132–1139.
[31] Q. Wang, Y. Wang, J. Ding, C. Wang, X. Zhou, W. Gao, H. Huang, F. Shao, Z. Liu, A bioorthogonal system reveals antitumour immune function of pyroptosis, Nature 579 (7799) (2020) 421–426.
[32] S. Ruhl, K. Shkarina, B. Demarco, R. Heilig, J.C. Santos, P. Broz, ESCRT-dependent membrane repair negatively regulates pyroptosis downstream of GSDMD activation, Science 362 (6417) (2018) 956–960.
[33] G. Li, S. Liu, Y. Chen, J. Zhao, H. Xu, J. Weng, F. Yu, A. Xiong, A. Udduttula, D. Wang, P. Liu, Y. Chen, H. Zeng, An injectable liposome-anchored teriparatide incorporated gallic acid-grafted gelatin hydrogel for osteoarthritis treatment, Nat. Commun. 14 (1) (2023) 3159.

[34] K. Li, H. Liu, W. Gao, M. Chen, Y. Zeng, J. Liu, L. Xu, D. Wu, Mulberry-like dual-drug complicated nanocarriers assembled with apogossypolone amphiphilic starch micelles and doxorubicin hyaluronic acid nanoparticles for tumor combination and targeted therapy, Biomaterials 39 (2015) 131–144.
[35] T. Zhu, Z. Chen, G. Jiang, X. Huang, Sequential targeting hybrid nanovesicles composed of chimeric antigen receptor T-cell-derived exosomes and liposomes for enhanced cancer immunochemotherapy, ACS Nano 17 (17) (2023) 16770–16786.
[36] S. Dutta, B. Watson, S. Mattoo, J. Rochet, Calcein release assay to measure membrane permeabilization by recombinant alpha-synuclein, Bio-protocol 10 (14) (2020).
[37] S. Okada, B. Bartelle, N. Li, V. Breton-Provencher, J. Lee, E. Rodriguez, J. Melican, M. Sur, A. Jasanoff, Calcium-dependent molecular fMRI using a magnetic nanosensor, Nat. Nanotechnol. 13 (6) (2018) 473–477.
[38] J. Wallner, G. Lhota, D. Jeschek, A. Mader, K. Vorauer-Uhl, Application of Bio-Layer Interferometry for the analysis of protein/liposome interactions, J. Pharm. Biomed. Anal. 72 (2013) 150–154.
[39] J. Zhang, B. Gao, B. Ye, Z. Sun, Z. Qian, L. Yu, Y. Bi, L. Ma, Y. Ding, Y. Du, W. Wang, Z. Mao, Mitochondrial-Targeted delivery of polyphenol-mediated antioxidases complexes against pyroptosis and inflammatory diseases, Adv. Mater. 35 (11) (2023) e2208571.
[40] N. Mor-Vaknin, A. Saha, M. Legendre, C. Carmona-Rivera, M. Amin, B. Rabquer, M. Gonzales-Hernandez, J. Jorns, S. Mohan, S. Yalavarthi, D. Pai, K. Angevine, S. Almburg, J. Knight, B. Adams, A. Koch, D. Fox, D. Engelke, M. Kaplan, D. Markovitz, DEK-targeting DNA aptamers as therapeutics for inflammatory arthritis, Nat. Commun. 8 (2017) 14252.
[41] M. Hou, Y. Wei, Z. Zhao, W. Han, R. Zhou, Y. Zhou, Y. Zheng, L. Yin, Immuno-engineered nanodecoys for the multi-target anti-inflammatory treatment of autoimmune diseases, Adv. Mater. 34 (12) (2022) e2108817.
[42] B. Shan, Y. Zhou, M. Yin, Y. Deng, C. Ge, Z. Liu, R. Zhou, Q. Dong, X. Zhou, L. Yin, Macrophage membrane-reversibly cloaked nanotherapeutics for the anti-inflammatory and antioxidant treatment of rheumatoid arthritis, Small Methods 7 (9) (2023) e2300667.
[43] N. Feng, L. Liang, M. Fan, Y. Du, C. Chen, R. Jiang, D. Yu, Y. Yang, M. Zhang, L. Deng, X. Li, N. Geng, M. Xian, Q. Qin, X. Li, Q. Tan, F. Luo, F. Song, H. Qi, Y. Xie, F. Guo, Treating autoimmune inflammatory diseases with an siERN1-nanoprodrug that mediates macrophage polarization and blocks toll-like receptor signaling, ACS Nano 15 (10) (2021) 15874–15891.
[44] S. Wirtz, V. Popp, M. Kindermann, K. Gerlach, B. Weigmann, S. Fichtner-Feigl, M. Neurath, Chemically induced mouse models of acute and chronic intestinal inflammation, Nat. Protoc. 12 (7) (2017) 1295–1309.